ECCOMAS Congress 2016
VII European Congress on Computational Methods in Applied Sciences and Engineering
M. Papadrakakis, V. Papadopoulos, G. Stefanou, V. Plevris (eds.)
Crete Island, Greece, 5–10 June 2016

COUPLING OF FLUID STRUCTURE INTERACTION SOLVER WITH A VOF METHOD FOR MULTIPHASE STRUCTURE INTERACTION

D. Cerroni[1*], R. Da Vià[1], S. Manservisi[1] and F. Menghini[1]

[1]University of Bologna
Via dei Colli 16, Laboratory of Montecuccolino - DIN

[*] e-mail: daniele.cerroni2@unibo.it

Keywords: Fluid Structure Interaction, Volume of Fluid method, Multiphase flows

Abstract. *In this work we propose a preliminary model to study the deformation of solid structures induced by the interaction with a two-phase flow. The study of Fluid Structure Interaction and multiphase problems is of great interest because of many potential applications ranging from the biomedical field to the pressure tank design. We use a monolithic approach for the FSI problem while a Volume Of Fluid method (VOF) is considered for the reconstruction and the advection of the multiphase interface. An unstructured, time dependent computational grid and a fine Cartesian mesh are used for the FSI and the VOF problem, respectively. The interaction between the two different grids is obtained by projecting the velocity and the displacement field into the Cartesian grid and the color function into the unstructured mesh. This projection is performed with the MEDmem libraries included in the Salome platform. Concerning the VOF method, for an accurate reconstruction of the interface a huge number of computational elements are required and a multilevel algorithm coupled to an efficient compression-expansion technique is developed to reduce computational costs and memory requirements. After the mathematical description of the problems we test the proposed algorithm with different cases where the solid domain undergoes to both small and large deformation.*

1 INTRODUCTION

In recent years Fluid Structure Interaction (FSI) problems have gained attention in the computational field because of the improvement in computer performance and an increasing interest in more realistic modeling [17, 12]. Among all the applications, these computational techniques can be employed in biomedical field where the interaction between a fluid and a solid such as the blood and the artery wall, is of great importance. In a classic FSI problem a solid structure interacts with a single phase fluid. Few works can be found in literature where Multiphase Fluid Structure problems are considered. Two-phase flows are of great interest in several physical and industrial applications. In recent years such interest inspired the development of several numerical algorithms for the efficient and accurate simulation of multiphase flows. These algorithms include efficient solvers of the incompressible Navier-Stokes equations, stable and accurate techniques for the advection and reconstruction of the fluid interface and methods for the correct computation of surface tension forces. These algorithms can be classified in two categories considering how the computational grid is handled. In the first group moving grids are used [14]. The interface between the two phases always lies over the cell boundaries, which are continuously advected by following the flow motion. This representation allows a precise modeling of the fluid property discontinuities, and also a correct location of the capillary force, which is a singular term in the Navier-Stokes equations. Despite these good properties, moving grid methods can be used only when the general motion does not affect the topology of the computational grid, since severe grid stretching brings loss of accuracy in the discretization of the Navier-Stokes equations. Furthermore, since breaking or merging of drops and bubbles are almost impossible, a continuous re-meshing of the computational domain is required.

In the second group fixed grids are used. The interface points cross the cell boundaries and a numerical algorithm is then required to reconstruct its motion in the computational domain. The fluid properties are evaluated in the interface cells as an average between the properties of each phase. The capillary force, which is physically located only on the interface, is redistributed inside the cells cut by the interface. With this representation, severe deformations of the interface can be tracked without the need for re-meshing. For these reasons fixed grid methods are widely used. Fixed-grid methods for two-phase flows can be either Eulerian or Lagrangian. Eulerian front capturing schemes include volume-of-fluid (VOF), level set and phase field methods [16]. All these methods are based on a single scalar function defined in every grid cell. The phase motion can be followed during the simulation with a good conservation of mass, however the interface and all its geometrical information are usually poorly represented, especially in regions with high curvature. Moreover, filaments are usually artificially broken when their thickness becomes comparable to the grid spacing.

Lagrangian techniques, either front-tracking schemes with surface markers or with volume particles, maintain filamentary structures better than Eulerian methods and conserve mass adequately, even without explicit volume conservation constraints [1, 9]. Both the surface markers and the volume particles are moved along the flow characteristics, resulting in a more accurate description of the interface and its geometrical properties, such as the normal vector and the curvature. This representation allows for a very accurate volume conservation and interface advection even in situations where strong deformations of the interface are present. On the other hand, these schemes can be rather expensive,

as the number of markers or volume particles increases, or are associated to practical difficulties. These includes the need to keep logical connections among surface elements and the careful handling of drop breaking and merging. Fixed grid methods provide good solutions to the problem of interface advection. However the accurate representation of surface forces remains a problem since these forces are not located on the cell boundaries. The multiphase flow motion satisfies the Navier-Stokes equations, and it should be determined while taking into account the discontinuities of the fluid properties across the interface. Such discontinuities, together with high Reynolds numbers, may induce several numerical instabilities.

The coupling between a FSI and a VOF solver allows to increase dramatically the range of problems that can be studied. For example, deformation of offshore platforms or offshore wind farm due to water waves or the interaction between water and ship hulls can be simulated in a very realistic way. In order to couple the two problems many strategies can be employed, as an example, the first code output field can be written on a file and the other code can be run with this file as input and vice versa. This technique is simple and fast to implement but unfortunately it can be very slow because of the large time needed by writing and reading files. A more efficient and fast coupling can be obtained through dedicated libraries for the data exchange, like the MEDmem libraries implemented in the SALOME computational platform [2, 18].

In this work we consider Fluid Structure Interaction problems in which the fluid part is composed of two phases [11, 6]. For the reconstruction and advection of the interface we employ a front-tracking Volume of Fluid method [19, 13]. The coupling between the two solvers is performed using the MEDmem libraries for data exchange. In the next Section the mathematical model for a Multiphase Fluid Structure Interaction problem is presented. In the last Section some numerical results are show.

2 MATHEMATICAL MODEL

2.1 FSI problem

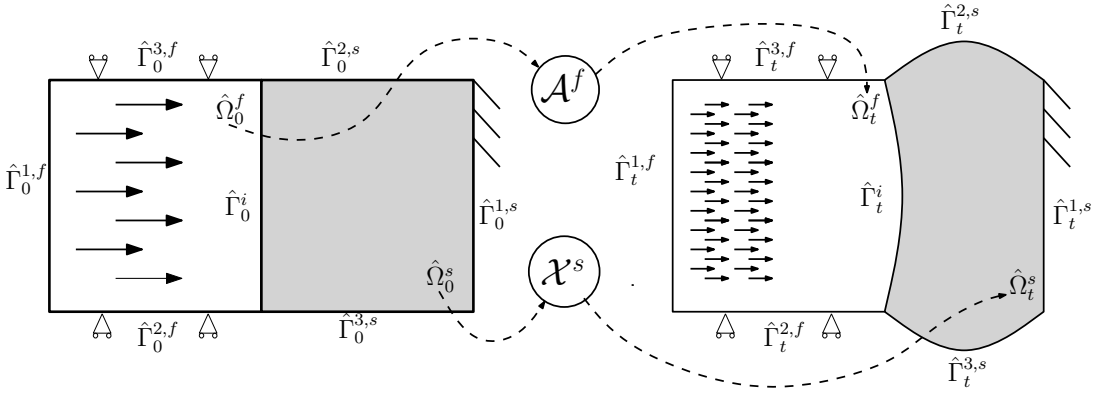

Figure 1: Reference and current configuration where a vessel wall interacts with a fluid.

In this Section we introduce the mathematical model for a generic Fluid Structure Interaction problem. In an ordinary FSI problem we consider a mechanical system composed by a laminar Newtonian fluid region and a solid one which defines a moving domain Ω_t. A schematic geometry of the problem is shown in Figure 1. Let Ω_t^f and Ω_t^s be the fluid and the solid region at $t \in (0, T]$, respectively. At $t = 0$ the fluid and solid region

are defined by $\hat{\Omega}_0^f$ and $\hat{\Omega}_0^s$. Let $\Gamma_t^i = \bar{\Omega}_t^f \cap \bar{\Omega}_t^s$ and $\hat{\Gamma}_0^i = \bar{\Omega}_0^f \cap \bar{\Omega}_0^s$ be the interface where solid and fluid interact. $\Gamma_t^k, k = 1, 2, 3$ and $\hat{\Gamma}_0^k, k = 1, 2, 3$ are defined to be the remaining external boundaries at $t \in (0, T]$ and $t = 0$, respectively. The evolution of the solid and fluid domain $\hat{\Omega}_0^f$ and $\hat{\Omega}_0^s$ are defined by

$$\mathcal{X}^s : \hat{\Omega}_0^s \times \mathbb{R}^+ \to \mathbb{R}^3 ,$$
$$\mathcal{A}^f : \hat{\Omega}_0^f \times \mathbb{R}^+ \to \mathbb{R}^3 ,$$

such that the range of $\mathcal{X}^s(\cdot, t)$ and $\mathcal{A}^f(\cdot, t)$ define Ω_t^s and Ω_t^f, respectively. $\mathcal{X}^s$ maps any material point $\hat{\mathbf{x}}_0^s$ from the given fixed reference configuration $\hat{\Omega}_0^s$ to the current solid material configuration Ω_t^s. The solid displacement is then defined as

$$\hat{\mathbf{u}}^s(\hat{\mathbf{x}}_0^s, t) = \mathcal{X}(\hat{\mathbf{x}}_0^s, t) - \hat{\mathbf{x}}_0^s . \tag{1}$$

The mapping $\mathcal{A}^f$ is such that $\mathcal{A}^f(\hat{\mathbf{x}}_0^f, t) = \hat{\mathbf{x}}_0^f + \hat{\mathbf{u}}^f(\hat{\mathbf{x}}_0^f, t)$, where $\hat{\mathbf{u}}^f(\hat{\mathbf{x}}_0^f, t)$ is defined as an arbitrary extension operator over the fluid domain $\hat{\Omega}_0^f$ and given by

$$\hat{\mathbf{u}}^f(\hat{\mathbf{x}}_0^f, t) = \mathrm{Ext}(\hat{\mathbf{u}}^s|_{\hat{\Gamma}_0^i}) \quad \text{in} \quad \hat{\Omega}_0^f . \tag{2}$$

The extension operator used to evaluate the fluid region displacement is the harmonic or Laplace operator. Other similar operators can be employed as described in [15, 12, 5]. The velocity $\hat{\mathbf{w}}^f$ is defined by

$$\hat{\mathbf{w}}^f = \frac{\partial \hat{\mathbf{u}}^f}{\partial t} \quad \text{in} \quad \hat{\Omega}_0^f . \tag{3}$$

This quantity represents the velocity in terms of the reference coordinate $\hat{\mathbf{x}}_0^f$. The behavior of the fluid is described by the Navier-Stokes equations for incompressible flows. For details the interested reader can also see [20, 10].

$$\begin{aligned}
&\rho^f \frac{\partial \mathbf{v}^f}{\partial t}\bigg|_{\tilde{\mathcal{A}}} + \rho^f \left(\mathbf{v}^f - \mathbf{w}^f\right) \cdot \boldsymbol{\nabla} \mathbf{v}^f - \boldsymbol{\nabla} \cdot \boldsymbol{\sigma}^f = \rho^f \mathbf{g} && \text{in} \quad (0, T) \times \Omega_t^f , \\
&\boldsymbol{\nabla} \cdot \mathbf{v}^f = \mathbf{0} && \text{in} \quad (0, T) \times \Omega_t^f , \\
&\mathbf{v}^f|_{t=0} = \mathbf{v}_0 && \text{in} \quad \hat{\Omega}_0^f , \\
&\mathbf{v}^f|_{\Gamma_{t,D}^{1,f} \cup \Gamma_{t,D}^{2,f}} = \mathbf{g}^f && \text{in} \quad (0, T) , \\
&\boldsymbol{\sigma}_f \cdot \mathbf{n}^f|_{\Gamma_{t,N}^{1,f} \cup \Gamma_{t,}^{2,f}} = \mathbf{h}^f && \text{in} \quad (0, T) ,
\end{aligned} \tag{4}$$

where ρ^f is the constant density, $\mathbf{v}^f$ is the fluid velocity, $\mathbf{g}$ is the gravity acceleration vector, $\tilde{\mathcal{A}}$ denotes the ALE application that maps the reference fluid configuration $\hat{\Omega}_0^f$ onto the current fluid configuration Ω_t^f and $\mathbf{w}^f$ denotes the fluid domain velocity. $\mathbf{n}$ is the unit normal vector that points outward from the boundary $\partial\Omega_t^f$ and $\mathbf{g}^f$, $\mathbf{h}^f$, $\mathbf{v}_0$ are given data. The flow state variables in the incompressible case are the pressure p^f and the velocity $\mathbf{v}^f$. The contribution of external forces such as gravity is assumed to be negligible. The constitutive relation for the stress tensor in the Newtonian incompressible case reads

$$\boldsymbol{\sigma}^f = -p^f \mathbf{I} + \boldsymbol{\tau}^f = -p^f \mathbf{I} + 2\mu^f \boldsymbol{\epsilon}\left(\mathbf{v}^f\right) , \tag{5}$$

where μ^f is the dynamic viscosity of the fluid, p^f the Lagrange multiplier associated to the incompressibility constraint and $\boldsymbol{\epsilon}\left(\mathbf{v}^f\right)$ the strain rate tensor defined as

$$\boldsymbol{\epsilon}\left(\mathbf{v}^f\right) = \frac{1}{2}\left(\boldsymbol{\nabla}\mathbf{v}^f + \left(\boldsymbol{\nabla}\mathbf{v}^f\right)^{\mathrm{t}}\right) . \tag{6}$$

The total time derivative is related to the adopted reference systems. The governing equations for structural mechanics are the following momentum equations

$$\rho^s \frac{\partial \mathbf{v}^s}{\partial t} - \boldsymbol{\nabla}\cdot\boldsymbol{\sigma}^s(\mathbf{u}^s) = \mathbf{0} \qquad \text{in} \quad \Omega_t^s \,, \tag{7}$$

where ρ^s is the density of the solid material, $\mathbf{v}^s$ is the velocity field and $\boldsymbol{\sigma}^s$ its Cauchy stress tensor, which is a function of the solid region displacement $\mathbf{u}^s$. Since the constitutive law for the solid stress tensor is expressed in terms of displacements one must solve both the balance equations (7) and the kinematic relation

$$\mathbf{v}^s = \frac{\partial \mathbf{u}^s}{\partial t} \,. \tag{8}$$

For the reference configuration we can introduce the right Cauchy-Green deformation tensor $\mathbf{C}$ as

$$C_{ij} = F_{ki}F_{kj} \qquad\qquad \forall\, i,j = 1,\ldots,3 \,, \tag{9}$$

where $\mathbf{F}$ is the deformation gradient tensor defined by $\mathbf{F} = \mathbf{I} + \boldsymbol{\nabla}\mathbf{u}^s$. In a similar way in the current configuration we can introduce the left Cauchy-Green deformation tensor, $\mathbf{b}$, as

$$b_{ij} = F_{ik}F_{jk} \qquad\qquad \forall\, i,j = 1,\ldots,3 \,. \tag{10}$$

According with this notation we can now express the Cauchy stress tensor, $\boldsymbol{\sigma}^s$, as [20]

$$\sigma^s_{ij} = \frac{2}{J}\left[b_{ij}\left(I\, b_{ij} - b_{im}b_{mj}\right)\frac{J\delta_{ij}}{2}\right]\begin{pmatrix}\frac{\partial W}{\partial I}\\ \\ \frac{\partial W}{\partial II}\\ \\ \frac{\partial W}{\partial J}\end{pmatrix} , \tag{11}$$

where $I = C_{ii}$, $II = 1/2\,(I - C_{ij}C_{ji})$ are the first and second invariant of the right Cauchy-Green strain tensor $\mathbf{C}$ and J its determinant. The quantity $W = W(I, II, J)$ is the strain energy of the system which depends on the constitutive law of the considered material. For example for a Neo-Hookian material, with respect to the current configuration, the energy function is defined by

$$\begin{aligned} W(I,J) =& \frac{1}{2}\mu_s\left(J^{-2/3}\mathrm{tr}\mathbf{C} - 3\right) + \\ & \frac{1}{2}\left(\lambda + \frac{2}{3}\mu_s\right)\left(\frac{1}{2}(J^2-1) - \ln J\right) . \end{aligned} \tag{12}$$

In the case of incompressible solid, the third invariant is equal to one so the energy density function becomes

$$W(I,J) = \frac{1}{2}\mu_s\left(\mathrm{tr}\mathbf{C} - 3\right) \tag{13}$$

and the Cauchy stress tensor is defined by

$$\boldsymbol{\sigma}^s = -p^s \mathbf{I} + \boldsymbol{\sigma}^{s*}\,, \tag{14}$$

where $\boldsymbol{\sigma}^{s*}$ is the tensor obtained by using the equations (11) and (13). The problem defined by (4)-(7) is not well posed since we have not yet prescribed any boundary conditions at the interface Γ_t^i. The coupling between the fluid and the solid model determines the missing boundary conditions, which consist of imposing the continuity of velocity and stress at the interface Γ_t^i as

$$\mathbf{v}^f|_{\Gamma_t^i} = \mathbf{v}^s|_{\Gamma_t^i}\,, \tag{15}$$

$$\boldsymbol{\sigma}^f \cdot \mathbf{n}^f|_{\Gamma_t^i} + \boldsymbol{\sigma}^s \cdot \mathbf{n}^s|_{\Gamma_t^i} = \mathbf{0}\,. \tag{16}$$

In order to write the weak formulation of the coupled problem, let us consider the following functional spaces

$$\begin{aligned}
\mathbf{V}^t &= \{\boldsymbol{\phi} \in \mathbf{H}^1(\Omega_t^f) : \boldsymbol{\phi}|_{\Gamma_{t,D}^{1,f} \cup \Gamma_{t,D}^{2,f}} = \mathbf{0}\}\,,\\
\mathbf{V}_g^t &= \{\boldsymbol{\phi} \in \mathbf{H}^1(\Omega_t^f) : \boldsymbol{\phi}|_{\Gamma_{t,D}^{1,f} \cup \Gamma_{t,D}^{2,f}} = \mathbf{g}^f\}\,,\\
Q^t &= L^2(\Omega_t^f)\,,\\
\mathbf{M}^0 &= \{\boldsymbol{\psi} \in \mathbf{H}^1(\hat{\Omega}_0^s) : \boldsymbol{\psi}|_{\hat{\Gamma}_{0,D}^{1,s} \cup \hat{\Gamma}_{0,D}^{2,s} \cup \hat{\Gamma}_{0,D}^{3}} = \mathbf{0}\}\,,\\
\mathbf{M}_g^0 &= \{\boldsymbol{\psi} \in \mathbf{H}^1(\hat{\Omega}_0^s) : \boldsymbol{\psi}|_{\hat{\Gamma}_{0,D}^{1,s} \cup \hat{\Gamma}_{0,D}^{2,s} \cup \hat{\Gamma}_{0,D}^{3}} = \mathbf{g}^s\}\,,\\
D^0 &= L^2(\hat{\Omega}_0^s)\,,
\end{aligned}$$

where $\mathbf{H}^1(\Omega)$ is the standard Sobolev space of order s with respect to the set Ω and $L^2(\Omega)$ is the Sobolev space of order 0 containing square integrable functions over Ω. For details concerning these function spaces one may consult [8]. In addition, let us introduce the following bilinear form

$$a^f(\mathbf{v}^\mathbf{f}, \boldsymbol{\phi}) = \int_{\Omega^f} \boldsymbol{\tau}^f(\mathbf{v}^f) : \boldsymbol{\nabla}\phi \, d\mathbf{x} = \mu(\boldsymbol{\nabla}\mathbf{v}^f + (\boldsymbol{\nabla}\mathbf{v}^f)^T, \boldsymbol{\nabla}\boldsymbol{\phi})\,, \tag{17}$$

where we denote with $\boldsymbol{\tau}^f$ the fluid viscosity tensor. The variational formulation of the fluid equations can be obtained through the usual method by multiplying the equations (4) with appropriate test functions, performing integrations on the whole domain and keeping into account the boundary and interface conditions. This procedure leads, for the velocity field $\mathbf{v} \in \mathbf{V}_g^t$ and pressure $p \in Q^t$, to the following fluid momentum equation

$$\begin{aligned}
&\rho^f \left(\left.\frac{\partial \mathbf{v}^f}{\partial t}\right|_{\tilde{\mathcal{A}}}, \boldsymbol{\phi} \right) + a(\mathbf{v}^f, \boldsymbol{\phi}) - \rho^f((\boldsymbol{\nabla}\cdot\mathbf{w}^f)\mathbf{v}^f, \boldsymbol{\phi}) + \rho^f(\left(\mathbf{v}^f - \mathbf{w}^f\right)\cdot\boldsymbol{\nabla}\mathbf{v}^f, \boldsymbol{\phi}) = \\
&\qquad (p^f, \boldsymbol{\nabla}\cdot\boldsymbol{\phi}) + \int_{\Gamma_t^i} (\boldsymbol{\sigma}^f\cdot\mathbf{n}^f)\cdot\boldsymbol{\phi}\, d\gamma + \int_{\Gamma_N^f} \mathbf{h}^f\cdot\boldsymbol{\phi}\, d\gamma + \int_{\Omega^f} \rho^f \mathbf{g}\cdot\boldsymbol{\phi}\, d\mathbf{x}\,, \qquad (18)\\
&(q, \boldsymbol{\nabla}\cdot\mathbf{v}^f) = 0\,,\\
&\mathbf{v}^f|_{t=0} = \mathbf{v}_0^f\,,
\end{aligned}$$

for all $\boldsymbol{\phi} \in \mathbf{V}^t$ and $q \in Q^t$. In a similar way, we define the following bilinear form

$$a^s(\mathbf{u}^s, \boldsymbol{\psi}) = (\boldsymbol{\sigma}^s(\mathbf{u}^\mathbf{s}), \boldsymbol{\nabla}\boldsymbol{\psi})\,. \tag{19}$$

By following the procedure briefly described above, we obtain at each time t, for the velocity $\mathbf{u}^s \circ \mathcal{X}^s \in \mathbf{M}_g^0$ and pressure $p^s \circ \mathcal{X}^s \in \mathbf{D}^0$, the following weak formulation for the solid problem

$$\begin{aligned}
&\rho^s \left(\frac{\partial^2}{\partial t^2} \mathbf{u}^s, \boldsymbol{\psi} \right) + a^s(\mathbf{u}^s, \boldsymbol{\psi}) - (p^s, \boldsymbol{\nabla} \cdot \boldsymbol{\psi}) = \int_{\Gamma_t^i} (\boldsymbol{\sigma}^s \cdot \mathbf{n}^s) \cdot \boldsymbol{\psi} \, d\gamma + \int_{\Gamma_N^s} \mathbf{h}^s \cdot \boldsymbol{\psi} \, d\gamma \,, \\
&(d, \boldsymbol{\nabla} \cdot \mathbf{u}^s) = 0 \,, \\
&\mathbf{u}^s|_{t=0} = \mathbf{u}_0^s \,, \qquad \mathbf{v}^s|_{t=0} = \mathbf{v}_0^s \,,
\end{aligned}$$

for all $\boldsymbol{\psi} \circ \mathcal{X}^s \in \mathbf{M}^0$ and $d \circ \mathcal{X}^s \in \mathbf{D}^0$. Let us introduce a global weak formulation for the fluid-structure problem. If we define the functional space

$$\mathbf{S}^t = \{ (\boldsymbol{\phi}, \boldsymbol{\psi} \circ \mathcal{X}^s) \in \mathbf{V}^t \times \mathbf{M}^0 : \boldsymbol{\psi}|_{\Gamma_t^i} = \boldsymbol{\phi}|_{\Gamma_t^i} \} \,, \tag{20}$$

from (15), (16), (18) and (20), we can write the FSI problem in the coupled formulation as

$$\begin{aligned}
&\rho^f \left(\left. \frac{\partial \mathbf{v}^f}{\partial t} \right|_{\tilde{\mathcal{A}}}, \boldsymbol{\varphi} \right) + a(\mathbf{v}^f, \boldsymbol{\varphi}) - \rho^f((\boldsymbol{\nabla} \cdot \mathbf{w}^f)\mathbf{v}^f, \boldsymbol{\varphi}) + \rho^f(\left(\mathbf{v}^f - \mathbf{w}^f\right) \cdot \boldsymbol{\nabla} \mathbf{v}^f, \boldsymbol{\varphi}) - \\
&\qquad (p^f, \boldsymbol{\nabla} \cdot \boldsymbol{\varphi}) + \rho^s(\frac{\partial^2}{\partial t^2} \mathbf{u}^s, \boldsymbol{\varphi}) + a^s(\mathbf{u}^s, \boldsymbol{\varphi}) - (p^s, \boldsymbol{\nabla} \cdot \boldsymbol{\varphi}) \qquad (21) \\
&\qquad\qquad - \int_{\Gamma_N^s} \mathbf{h}^s \cdot \boldsymbol{\varphi} \, d\gamma - \int_{\Gamma_N^f} \mathbf{h}^f \cdot \boldsymbol{\varphi} \, d\gamma = \int_{\Omega^f} \rho^f \mathbf{g} \cdot \boldsymbol{\varphi} \, d\mathbf{x} \,, \quad \forall \boldsymbol{\varphi} \in \mathbf{S}^t \\
&(q, \boldsymbol{\nabla} \cdot \mathbf{v}^f) = 0 \qquad (d, \boldsymbol{\nabla} \cdot \mathbf{u}^s) = 0 \,, \qquad (22) \\
&\mathbf{v}^f|_{t=0} = \mathbf{v}_0^f \qquad \mathbf{u}^s|_{t=0} = \mathbf{u}_0^s \qquad \mathbf{v}^s|_{t=0} = \mathbf{v}_0^s \,.
\end{aligned}$$

It is worth noting that by using the coupling conditions (15), (16) and this particular choice of the fluid-structure test functions, the boundary terms that appear in the fluid-solid interface Γ_t^i cancel out. This assures that forces at the interface are always computed in an exact way.

2.2 Multiphase problem

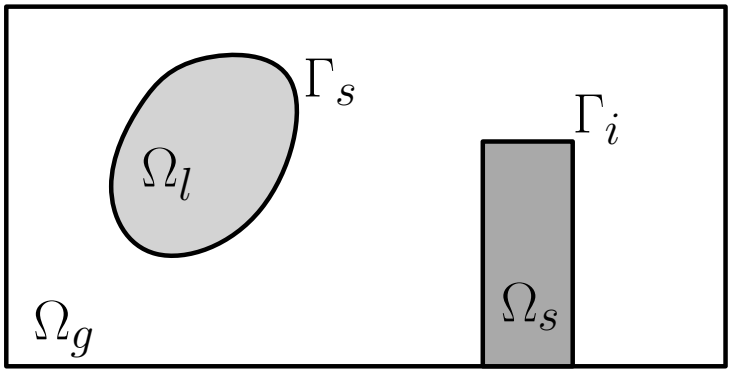

Figure 2: Computational domain. The liquid in Ω_l and Ω_l are the reference fluid phases and the boundary between the two fluid phases is denoted by Γ_s. Ω_s mark the solid region of the domain and the interface between the solid and the fluid region is labeled with Γ_i.

In this Section the mathematical model of the Multiphase Fluid Structure Interaction problem is presented. Let us consider a domain as shown in Figure 2, where Ω marks the whole domain, Ω_l is the portion of the domain occupied by the reference fluid phase and Ω_g is the sub-domain with the secondary phase. The boundary between the two immiscible fluids is denoted by Γ_s, and its topology can vary during the evolution of the system since each sub-domain evolves in time. The solid domain is labeled with Ω_s and the interface between the fluid phases and the solid region is marked Γ_i. As explained in Section 2.1 the balance equations that hold in a fluid structure interaction problem are

$$\rho^f \frac{\partial \mathbf{v}^f}{\partial t}\bigg|_{\tilde{\mathcal{A}}} + \rho^f \left(\mathbf{v}^f - \mathbf{w}^f\right) \cdot \boldsymbol{\nabla} \mathbf{v}^f - \boldsymbol{\nabla} \cdot \boldsymbol{\sigma}^f = \rho^f \mathbf{g} \qquad \text{in} \quad (0,T) \times \Omega_t^f \cup \Omega_t^g \,, \tag{23}$$

$$\rho^s \frac{\partial \mathbf{v}^s}{\partial t} - \boldsymbol{\nabla} \cdot \boldsymbol{\sigma}^s(\mathbf{u}^s) = \mathbf{0} \qquad \text{in} \quad (0,T) \times \Omega_t^s \,, \tag{24}$$

$$\boldsymbol{\nabla} \cdot \mathbf{v} = \mathbf{0} \qquad \text{in} \quad (0,T) \times \Omega_t \,, \tag{25}$$

$$\mathbf{v}^f|_{t=0} = \mathbf{v}_0 \qquad \text{in} \quad \hat{\Omega}_0 \,, \tag{26}$$

$$\mathbf{v}|_{\Gamma_{t,i}} = \mathbf{g}^f \qquad \text{in} \quad (0,T) \,, \tag{27}$$

$$\boldsymbol{\sigma} \cdot \mathbf{n}|_{\Gamma_{t,i}} = \mathbf{h}^f \qquad \text{in} \quad (0,T) \,. \tag{28}$$

In order to take into account the presence of a multiphase fluid that interacts with a solid domain, we modify the first equation of (23) while the rest of the problem is treated as described in the previous Section. The momentum balance equations in the fluid domain are formally written as in single phase formulation

$$\begin{aligned} &\rho^f \frac{\partial \mathbf{v}^f}{\partial t}\bigg|_{\tilde{\mathcal{A}}} + \rho^f \left(\mathbf{v}^f - \mathbf{w}^f\right) \cdot \boldsymbol{\nabla} \mathbf{v}^f - \nabla \cdot (\mu(\nabla \mathbf{v}^{\mathbf{f}} + (\nabla \mathbf{v}^{\mathbf{f}^\intercal})) + \nabla p = \rho^f \mathbf{g} \,, \\ &\nabla \cdot \mathbf{v}^{\mathbf{f}} = 0 \,, \qquad \mathbf{x} \in \Omega, t \in [0,T] \,, \end{aligned} \tag{29}$$

and the difference lies in the definition of the physical properties ρ^f and μ^f. If we denote with l the properties of the reference phase and with g the values associated to the secondary phase, we can define the physical properties ρ^f and μ^f as

$$\rho^f = \rho_l \chi + \rho_g (1 - \chi) \,, \tag{30}$$

$$\mu^f = \mu_l \chi + \mu_g (1 - \chi) \,, \tag{31}$$

where χ is the color or indicator function. This function describes the distribution of the two phases in the domain. It is equal to 1 in the reference phase and 0 in the secondary phase. We note that the function χ is discontinuous on the interface Γ_s. We can define χ as

$$\chi(\mathbf{x}, t) = \int_{\Omega_l(t)} \delta(\mathbf{x}' - \mathbf{x}) \, d\mathbf{x}' \quad \forall \mathbf{x} \in \Omega \,. \tag{32}$$

The indicator function is therefore a multidimensional Heaviside function that changes value on Γ_s. We can also write that

$$\nabla \chi = -\int_{\Gamma_s} \delta(\mathbf{x}' - \mathbf{x}) \mathbf{n}' \, dS' = -\mathbf{n} \int_{\Gamma_s} \delta(\mathbf{x}' - \mathbf{x}) \, dS' = -\mathbf{n} \delta_s(\mathbf{x}) \,, \tag{33}$$

where $\delta_s(\mathbf{x})$ is the Dirac delta function that is discontinuous on Γ_s. Under the hypotheses of immiscible fluids with no phase change, the color function behaves like a passive scalar

and is purely transported by the velocity field, following the simple advection equation

$$\frac{\partial \chi}{\partial t} + (\mathbf{v^f} \cdot \nabla)\chi = 0\,, \qquad \text{in } \Omega \times [0,T]\,. \tag{34}$$

The Volume of Fluid algorithm is employed to solve (34). Given an initial state of the indicator function (32) the VOF algorithm is implemented in two steps. First the interface is advected with an explicit Lagrangian advection method using the fluid velocity as computed by the FSI solver and the normal vector to the interface. Then the interface is reconstructed based on the color function gradient and on the conservation of volume constraint. In this work we use a Piecewise Linear Interface Calculation (PLIC) reconstruction scheme together with an ELVIRA method for the computation of the interface normals. For detailed information on this method the interested reader can consult [19, 13, 7, 4, 3].

3 NUMERICAL RESULTS

In this Section we report some numerical results obtained by implementing the mathematical model just described in a computational platform where the dedicated solvers for the FSI and the VOF problems are coupled. Inside this platform they can exchange data in a fast and efficient way. In all the test cases the fluid is composed of two phases with different densities and a portion of the domain is a solid region that undergoes to deformations due to the fluid motion. We use standard units of measure for all the results reported.

3.1 Test 1: Dam break

In this first test case we consider the dam break problem. This is a typical benchmark for two-phase flow simulations but in this case we consider a deformable solid on which the dam fluid impacts. The initial configuration of the problem is shown in Figure 3 in particular in the right part of this Figure one can see the solid, the primary and the secondary fluid regions marked by Ω_s, Ω_l, Ω_g, respectively. The global domain $\Omega = \Omega_s \cup \Omega_l \cup \Omega_g$ is the square $[0,1] \times [0,1]$. The geometries of the different parts of the domain are specified by giving the coordinate of some reference points. According to

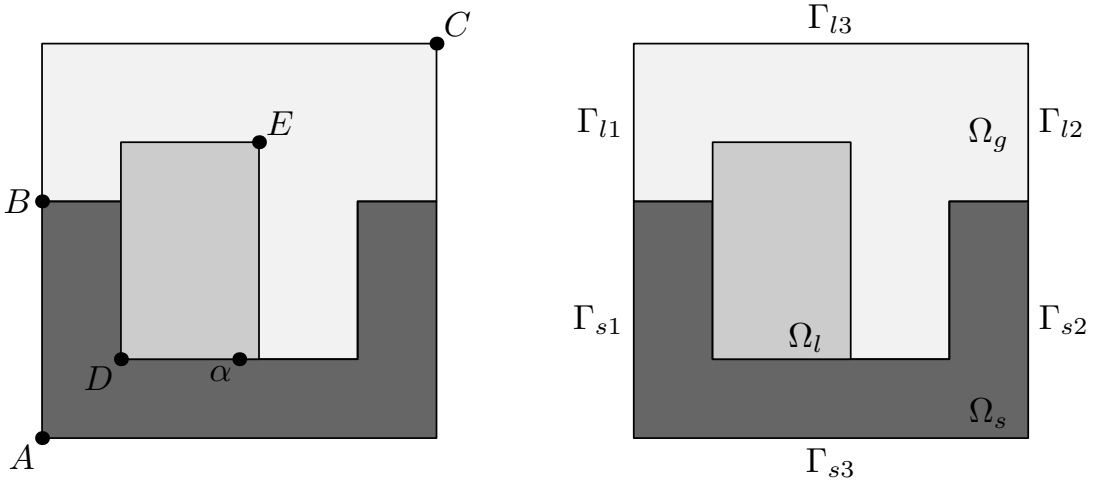

Figure 3: Test 1: Domain overview. On the left some reference points: $A = (0,0)$, $B = (0,0.6)$, $C = (1,1)$, $D = (0.2,0.2)$, $E = (0.5,0.7)$ and $\alpha = (0.2,0.5)$. On the right labeling of the surfaces.

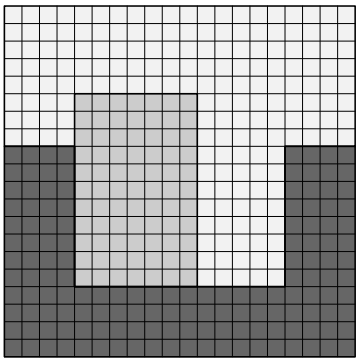

Parameter	Value
ρ_l, ρ_s	500 Kg/m^3
μ_l	0.005 Pa s
ρ_g/ρ_l	0.001
μ_g/μ_l	0.01
Young modulus	$4 \cdot 10^4$ Pa
Poisson coefficient	0.4

Figure 4: Test 1. Coarse computational grid on the left, physical parameters on the right.

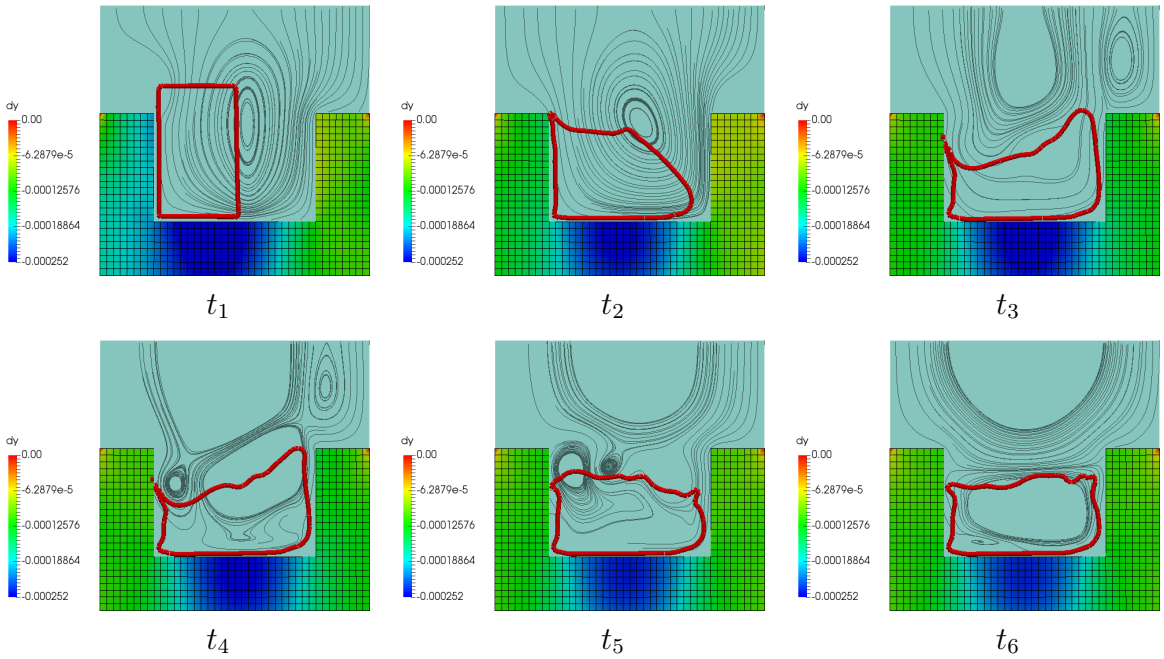

Figure 5: Test 1. Solution overview at different time steps: $t_1 = 0.005$ s, $t_2 = 0.04$ s, $t_3 = 0.08$ s, $t_4 = 0.095$ s, $t_5 = 0.16$ s and $t_6 = 0.2$ s.

the nomenclature shown on the left of Figure 3, the coordinate of the reference points in standard units of measure are: $A = (0, 0)$, $B = (0, 0.6)$, $C = (1, 1)$, $D = (0.2, 0.2)$ and $E = (0.5, 0.7)$. Due to the different densities of the two fluid phases (Ω_l and Ω_g) and the gravitational field, Ω_l falls down into the solid container Ω_s which deforms due to the interaction with both the fluid phases.

The coarse computational grid, both for the FSI and VOF modules, is generated subdividing Ω into 400 cells (20 subdivision per edge) and it is shown on the left of Figure 4. The coarse grid is then refined multiple times to allow for a proper grid resolution for the VOF solver. According to notation shown in Figure 3, we impose a vanishing velocity field on $\Gamma_{l1} \cup \Gamma_{l2}$ and at the boundary fluid structure interface $\{\Gamma_{l1} \cap \Gamma_{s1}\} \cup \{\Gamma_{l2} \cap \Gamma_{s2}\}$. A homogeneous Neumann condition is imposed of the fluid region Γ_{l3} and on the solid boundary Γ_{s3}. The physical properties of the different phases of the problem are summarized in the Table on the right of Figure 4, in particular both of the fluid phases are modeled as Newtonian incompressible fluids while the solid is represented by a compressible linear elastic material.

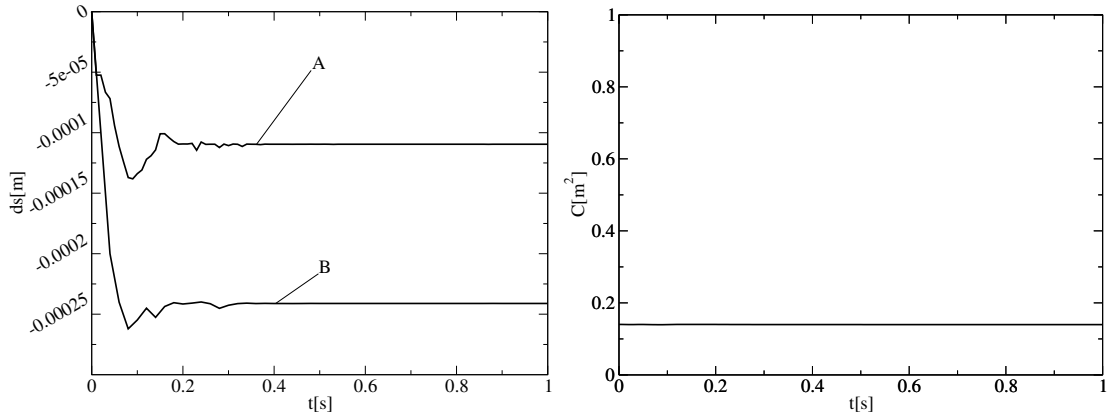

Figure 6: Test 1. On the left, transverse (A) and axial (B) displacement over time. On the right, color function integral over the computational domain over time.

In Figure 5 the solution overview is shown at different time step $t = 0.005$, 0.04, 0.08, 0.095, 0.16 and 0.2 s. In this Figure the axial displacement field is shown in the solid region (Ω_s) while in the fluid part we mark in red the interface between the primary and the primary phase and in light gray the streamlines of the fluid velocity field. We can notice that, as expected, the primary phase with higher density falls down into the solid container that is deformed due to its weight.

The transverse and axial displacements of point α (see left part of Figure 3) over time are shown in the left part of Figure 6 with curves A and B respectively. We can notice that the displacement field after some initial oscillations reaches a steady state configuration and it is always smaller than the characteristic length of the computational grid. In such condition the displacement field can be neglected in the projection of the velocity and the color function during the data exchange between the FSI and VOF meshes. In order to check the performance of the coupled FSI-VOF solver we can evaluate the primary phase volume by computing the color function integral

$$\int_{\Omega_l(t)} d\mathbf{x} = k\,. \tag{35}$$

We remark that the fluid is represented with an incompressible model so because of the free divergence constraint of the velocity field the total primary phase volume k must remain constant over time. The quantity k as computed from (35) is plotted over time on the right of Figure 6.

3.2 Test 2: Tank filling

In the second test case we consider a filling problem in which, as in the previous case, two fluid phases and a solid region are considered. The domain overview is shown in Figure 7, in particular on the left of that Figure the specific geometries of the different parts of the domain are specified by giving the coordinates of some reference points: $A = (0, 0)$, $B = (0.5, 0.15)$, $C = (0.5, 0.5)$ and $D = (1, 1)$. On the right of the same Figure one can see the solid, the primary and the secondary fluid regions marked as Ω_s, Ω_l, Ω_g, respectively. The global domain $\Omega = \Omega_s \cup \Omega_l \cup \Omega_g$ is a square with a surface of $1m^2$.

According to the surface labeling shown in Figure 7, we impose a vanishing velocity field on $\Gamma_{l1} \cup \Gamma_{l2} \cup \Gamma_{l3} \cup \Gamma_{s1} \cup \Gamma_{s2}$. A homogeneous Neumann condition is imposed on the solid region Γ_{s3}. Concerning the multiphase advection problem, the color function

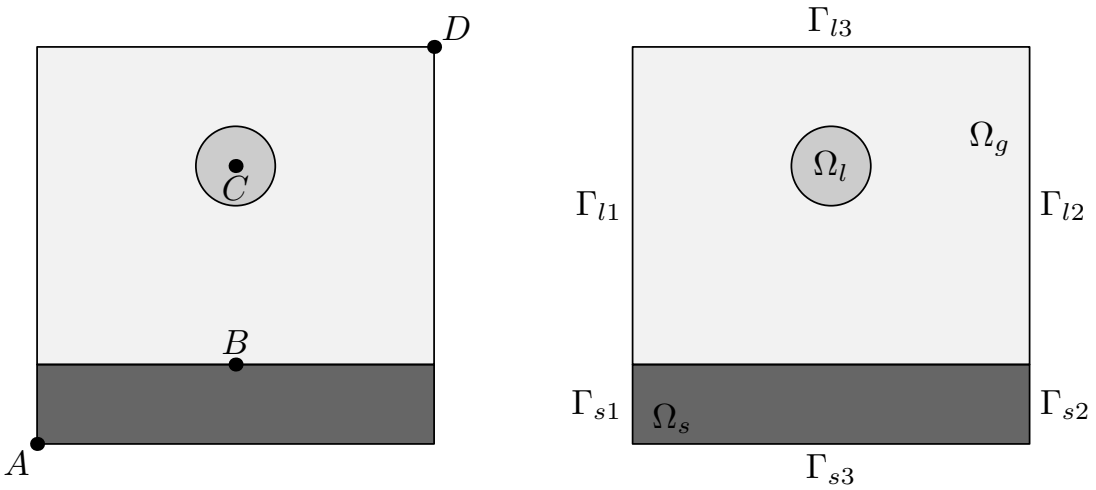

Figure 7: Test 2: Domain overview. On the left reference point: $A = (0m, 0m)$, $B = (0.5m, 0.15,)$, $C = (0.5m, 0.5m)$ and $D = (1m, 1m)$. On the right part labeling of the surfaces.

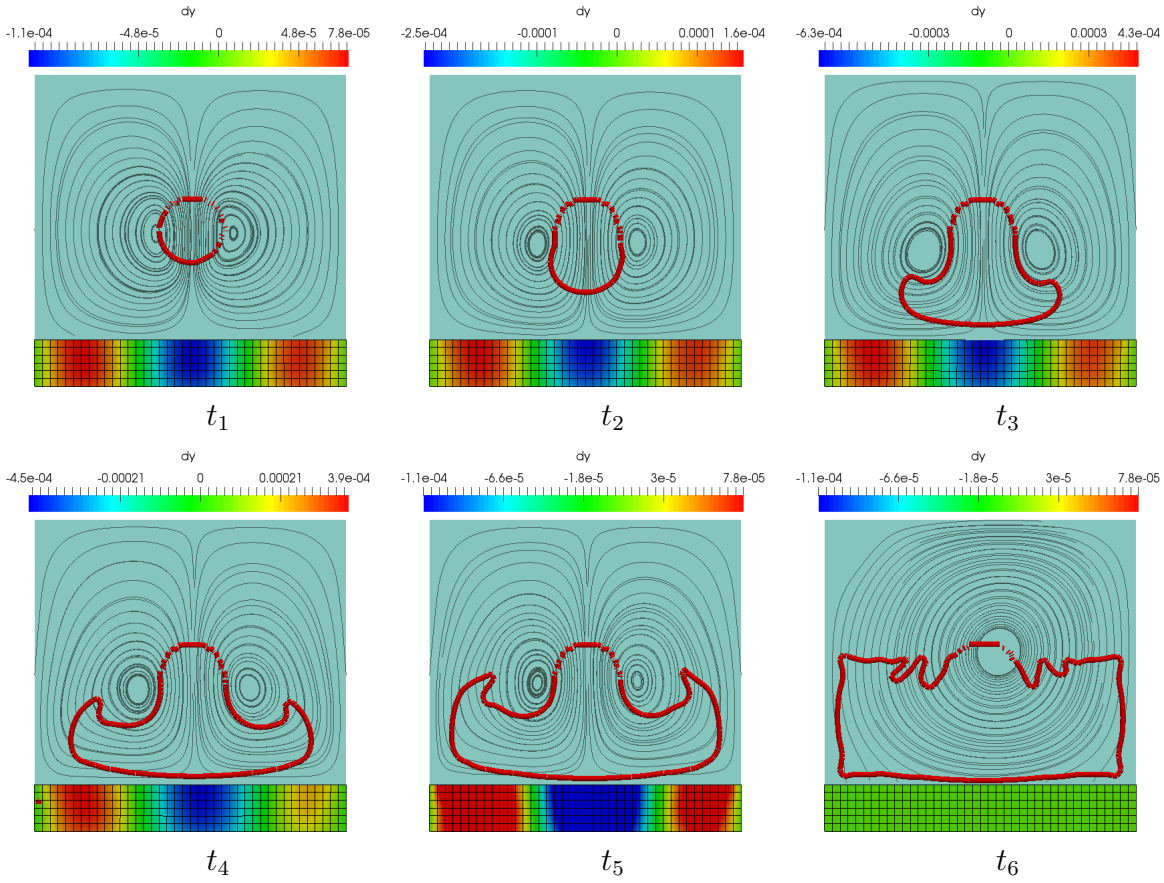

Figure 8: Test 12. Solution overview at different time steps: $t_1 = 0.005s$, $t_2 = 0.09s$, $t_3 = 0.2s$, $t_4 = 0.3s$, $t_5 = 0.4s$ and $t_6 = 2s$.

is set to 1 in the Ω_l region. The physical properties of the different materials present in the problem are the same used in the previous case and can be seen in the Table on the right of Figure 4. The color function is set to 1 in the Ω_l domain for the full time of the simulation, so this volume represents an inflow for the primary phase with velocity computed by the FSI solver. This phase flows inside the domain until it cover the circular

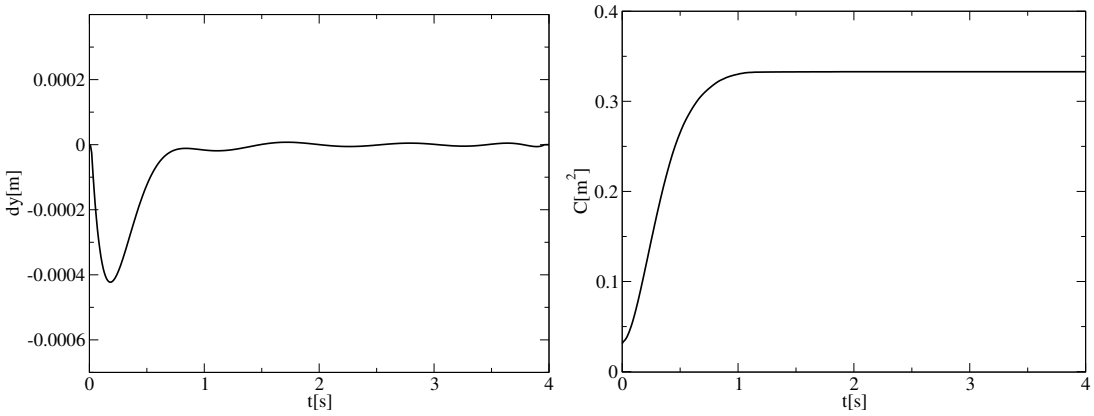

Figure 9: Test 2. On the left, axial displacement over time. On the right, color function integral over the computational domain over time.

inlet region and a steady state configuration is reached.

In Figure 8 the solution overview is shown at different time steps $t = 0.005$, 0.09, 0.2, 0.3, 0.4 and 2 s. In the solid region Ω_s we report with colors the axial displacement field while in the fluid region $\Omega_l \cup \Omega_g$ we show the interface between the two phases $\Omega_l \cap \Omega_g$ as a red solid line. The streamlines of the fluid velocity field are reported in light gray in the same Figure. We can notice that as the heavy phase falls because of the gravitational field, more secondary phase is injected in the domain until it cover the inlet region. The axial displacement of the central point of the solid region over time is shown on the left of Figure 9. We can notice that the displacement field shows a great oscillation due to the first contact between the secondary phase and the solid region, after this impact the average axial deformation decreases and reaches a steady negative value when the injection of the secondary phase stops. Also in this case it is worth to notice that the deformations that occurs are always smaller than the characteristic length of the computational grid.

As in the previous case, in order to check the performance of the FSI-VOF coupled modules, we can evaluate the integrated color function (35). In this case because of the inlet of the primary phase the total primary phase volume k must increase over time. The result of (35) along time is shown on the right of Figure 9. we can notice that the value increases as the secondary phase is injected into the domain and reaches a steady value as the injection ends.

3.3 Test 3: Bending rod in two-phase flow

In this third test we consider the flow of a multiphase fluid around a solid deformable obstacle. The domain overview is shown on the left of Figure 10. The global domain is a cube characterized by an edge of 1 m, the obstacle is placed in the center of the cube base with a square transverse section a^2 of 0.01 m^2 and a height b of 0.5 m. The physical parameters employed for this test case are reported in Figure 10 on the right. In this Table we see that the fluid and the solid have the same density, while the density ratio between the primary and secondary phase is close to the water over air ratio. The solid has been modeled as an incompressible solid and the fluids with an incompressible Newtonian model.

The boundary and initial conditions of the problem can be seen in the set of Figures 11. In the colored surface of the sub figure a we set an homogeneous Neumann boundary condition to simulate the outlet of the domain. In the colored surfaces of sub figure

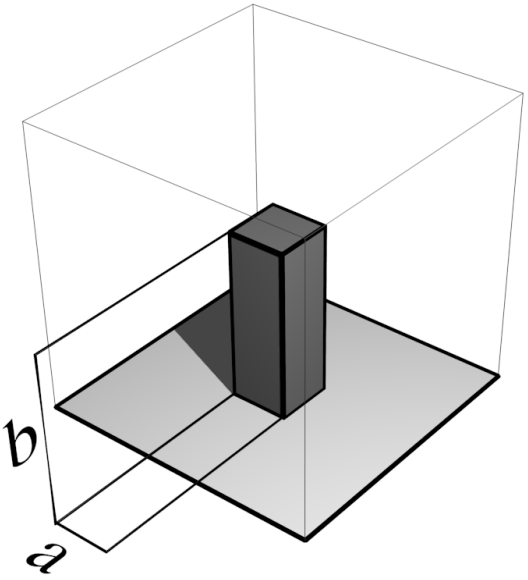

Parameter	Value
ρ_l, ρ_s	500 Kg/m^3
μ_l	0.005 Pa s
ρ_g/ρ_l	0.001
μ_g/μ_l	0.01
Young modulus	$4 \cdot 10^4$ Pa
Poisson coefficient	1/2

Figure 10: Test 3. Domains overview on the left and physical parameters on the right.

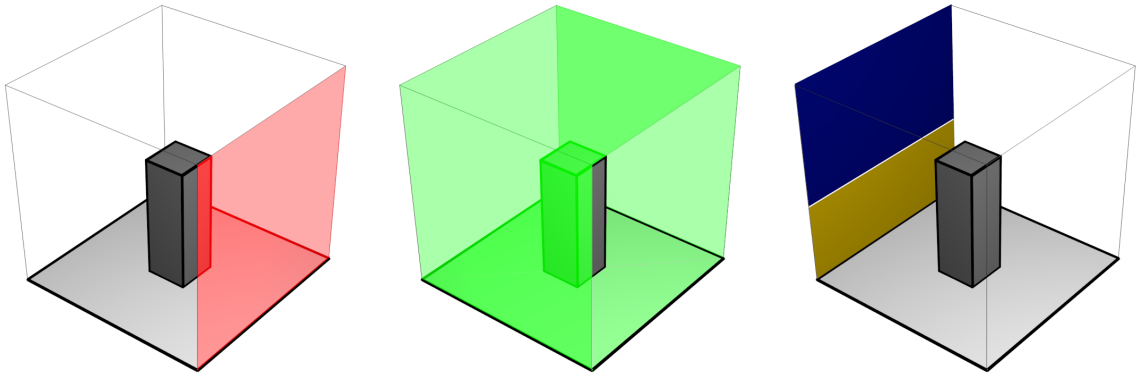

a *b* *c*

Figure 11: Test 3. Boundary conditions overview: *a* homogeneous Neuman, *b* homogeneous Dirichlet and *c* non homogeneous Dirichlet.

b we impose a no slip condition while in the colored surfaces of *c* a non homogeneous Dirichlet is set as an inlet. In that surface we impose a vanishing transverse velocity and a non-vanishing axial flows. In particular the fluid flows into the domain with a constant velocity of 1 m/s. Concerning the multiphase problem we consider a stratified flow with the primary heavy phase on the bottom and the secondary phase on top. As initial condition we consider the domain filled with the secondary phase while the boundary condition applied as inlet is visible in sub figure *c* of Figures 11. The yellow region is occupied by the primary phase with a height of 0.3 while in the blue region the secondary phase has a height of 0.7. During the simulation the heavy phase enters in the domain and flows on the bottom of the domain because of the gravity, following a typical stratified flow pattern.

In this test we consider the obstacle as a deformable solid rod, so the impact with the heavy phase displaces the rod with a force based on the weight and inertia of the fluid phase. One of the main interesting features of the coupled FSI-VOF solver is that the

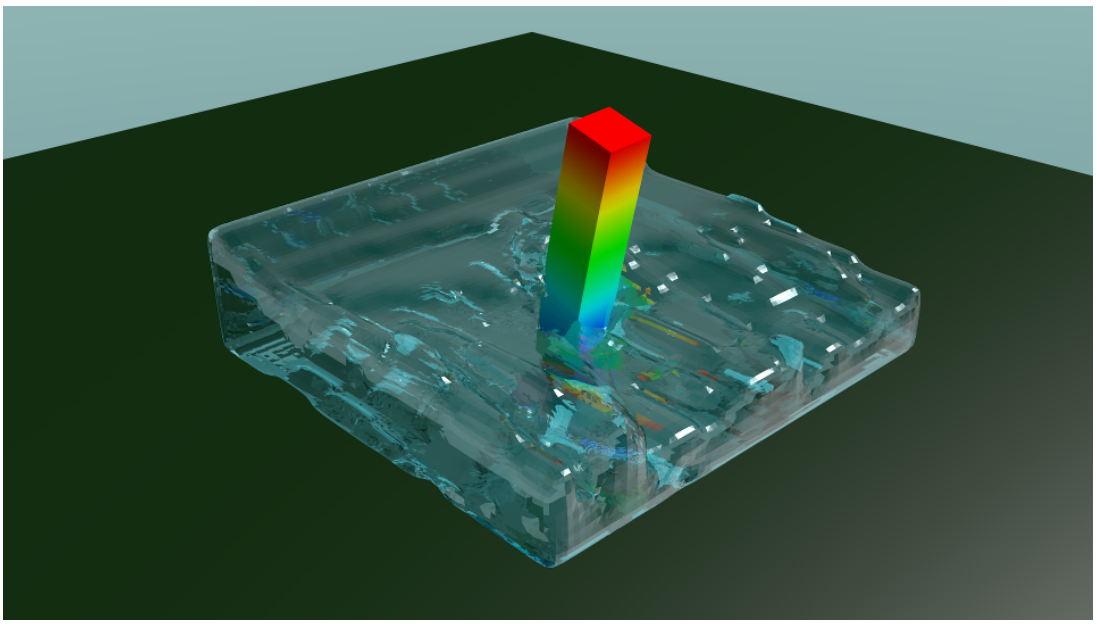

Figure 12: Test 3. Solution overview at $t = 10$ s.

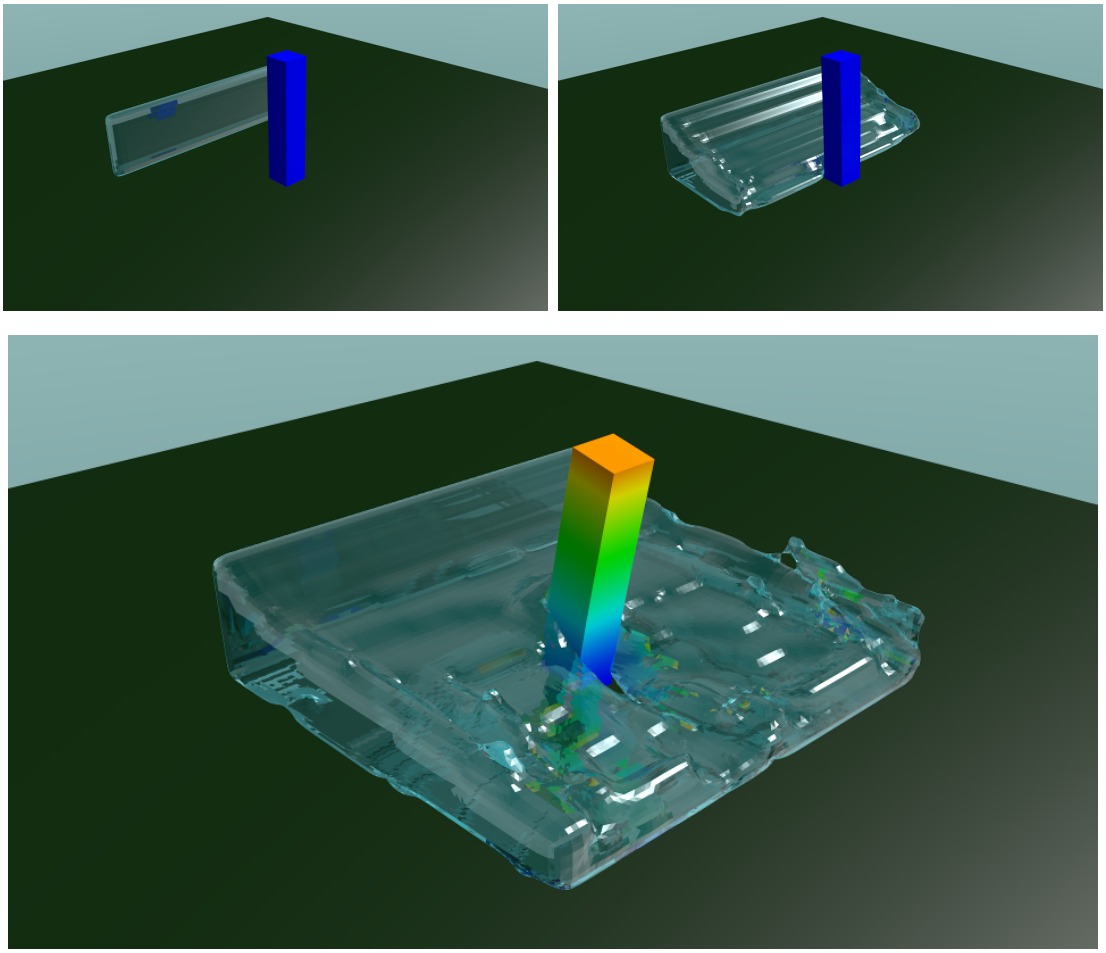

Figure 13: Simulation of the two-phase flow over a bending rod. From top left to bottom right three different time steps: $t_1 = 0.1$ s, $t_2 = 2.5$ s and $t_3 = 5$ s.

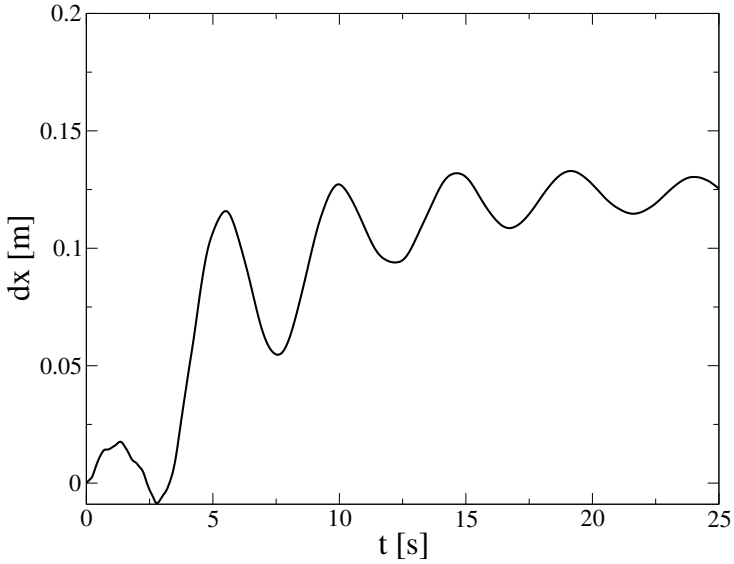

Figure 14: Displacement dx in the main flow direction on the most stressed point of the rod, reported as a function of time.

displacements of the solid can be precisely evaluated together with the stresses inside the structure. Moreover the bending of the solid has an influence on the flow field which could not be taken in consideration without the FSI solver.

In Figure 12 an overview of the solution is shown when the steady state condition is being approached. From this Figure we can see how the multiphase fluid flows into the computational domain and deforms the bending rod which is colored with the displacement in the main direction of the flow. The primary-secondary phase interface is represented with a transparent surface. In Figure 13 the solution overview is shown at different time steps: $t = 0.1$ s, $t_2 = 2.5$ s and $t_3 = 5$ s. From this sequence we can appreciate the evolution of the secondary phase flow together with the deformation of the bending rod. The color of the rod represents the displacement in the main flow direction. It can be seen that, due to the impact with the secondary phase, the rod bends and begins to oscillate. In Figure 14 the displacement of the central point of the top surface of the solid part in the main flow direction is reported as a function of time. The oscillating damped behavior of the rod in the main direction (x axis) can be clearly seen in this Figure. We remark that although the deformation in the top part of the rod are large, where the solid interact with the secondary phase the deformation field is still smaller then the characteristic length of the VOF grid. In such condition the displacement can be neglected in the projection of the computational fields among the different grids.

4 CONCLUSION

In this paper we have presented a model for the multiphase simulation of Fluid Structure Interaction problems based on a monolithic FSI approach and a Volume of Fluid method. The domain consists of a fluid and a solid region. Inside the fluid two phases are present with different physical properties. The solution of this problem is accomplished through the coupling of the FSI and VOF solvers using dedicated data exchange libraries. The results reported show that this method is capable to predict the displacements and stresses that a solid undergoes while interacting with a two phase fluid. Some improvements for future works could be to take into account the surface tension for the secondary

phase and consider cases where large displacements occur where the secondary phase is present.

REFERENCES

[1] F. Aubert, E. Aulisa, S. Manservisi, and R. Scardovelli. Interface tracking with dynamically-redistributed surface markers in unstructured quadrangular grids. *Computers & fluids*, 35 (10):1332–1343, 2006.

[2] J.P. Aubry. *Beginning with Code Aster. A Practical Introduction to Finite Element Method using CodeAster, Gmsh and Salome*. Framasoft, 2013.

[3] E. Aulisa, A. Cervone, S. Manservisi, and P. Seshaiyer. A multilevel domain decomposition approach for studying coupled flow applications. *Communications in Computational Physics*, 6(2):319–341, 2009.

[4] E. Aulisa, S. Manservisi, and P. Seshaiyer. A computational multilevel approach for solving 2d navier-stokes equations over non-matching grids. *Computer Methods in Applied Mechanics and Engineering*, 195(33-36):4604–4616, 2006.

[5] Daniele Cerroni, Sandro Manservisi, and Filippo Menghini. A new moving mesh technique for monolithic multigrid fluid-structure interaction solver. *Recent Advances in Civil Engineering and Mechanics*, 1:146–152, 2014.

[6] Daniele Cerroni, Sandro Manservisi, and Filippo Menghini. An improved monolithic multigrid Fluid-Structure Interaction solver with a new moving mesh technique. *International Journal of Mathematical Models and Methods in Applied Sciences*, 9:227–234, 2015.

[7] A Cervone, Sandro Manservisi, and Ruben Scardovelli. A fem solver coupled to a multilevel vof method for simulation of axisymmetric jets and to a front-tracking method for simulation of spreading droplets. *Atomization and Sprays*, 20(2), 2010.

[8] P.G. Ciarlet. *The finite element method for elliptic problems*, volume 40. Siam, 2002.

[9] J. Glimm, M. J. Graham, J. Grove, X. L. Li, T.M. Smith, D. Tan, F. Tangerman, and Q. Zhang. Front tracking in two and three dimensions. *Computers & Mathematics with Applications*, 35(7):1–11, 1998.

[10] Arthur Guittet, Maxime Theillard, and Frédéric Gibou. A stable projection method for the incompressible navier–stokes equations on arbitrary geometries and adaptive quad/octrees. *Journal of Computational Physics*, 292:215–238, 2015.

[11] Matthias Heil. An efficient solver for the fully coupled solution of large-displacement fluid–structure interaction problems. *Computer Methods in Applied Mechanics and Engineering*, 193(1):1–23, 2004.

[12] P. Le Tallec and J. Mouro. Fluid structure interaction with large structural displacements. *Computer Methods in Applied Mechanics and Engineering*, 190(24):3039–3067, 2001.

[13] J.E. Pilliod and E. G. Puckett. Second-order accurate volume-of-fluid algorithms for tracking material interfaces. *Journal of Computational Physics*, 199(2):465–502, 2004.

[14] G Ryskin and LG Leal. Numerical solution of free-boundary problems in fluid mechanics. part 1. the finite-difference technique. *Journal of Fluid Mechanics*, 148:1–17, 1984.

[15] PA Sackinger, PR Schunk, and RR Rao. A newton–raphson pseudo-solid domain mapping technique for free and moving boundary problems: a finite element implementation. *Journal of Computational Physics*, 125(1):83–103, 1996.

[16] Ruben Scardovelli and Stéphane Zaleski. Interface reconstruction with least-square fit and split eulerian–lagrangian advection. *International Journal for Numerical Methods in Fluids*, 41(3):251–274, 2003.

[17] T. Tezduyar, Y. Bazilevs, and K. Takizawa. *Computational Fluid-Structure Interaction*. Wiley, 2013.

[18] D. Thakore. *Finite Element Analysis using Open Source Software*. Moonish Enterprises, 2014.

[19] Grétar Tryggvason, Ruben Scardovelli, and Stéphane Zaleski. *Direct numerical simulations of gas–liquid multiphase flows*. Cambridge University Press, 2011.

[20] Olgierd Cecil Zienkiewicz, Robert Leroy Taylor, Olgierd Cecil Zienkiewicz, and Robert Lee Taylor. *The finite element method*, volume 3. McGraw-hill London, 1977.